Available online at www.sciencedirect.com
SCIENCE DIRECT®
Journal of Solid State Chemistry 178 (2005) 1452–1463
JOURNAL OF SOLID STATE CHEMISTRY
www.elsevier.com/locate/jssc

Structural studies in the $BaO–B_2O_3–TiO_2$ system by XAS and ^{11}B-NMR

L.J.Q. Maia[a], V.R. Mastelaro[a,*], J.F. Schneider[a], P. Parent[b], C. Laffon[b]

[a]*Instituto de Física de São Carlos, Universidade de São Paulo, Avenida Trabalhador Saocarlense 400, C.P. 369, 13560-970, São Carlos, SP, Brazil*
[b]*Laboratoire pour l'Utilisation du Rayonnement Electromagnétique (LURE), Centre Universitaire Paris-Sud, Bât. 209d, BP 34, 91898 Orsay Cedex, France*

Received 16 December 2004; received in revised form 17 February 2005; accepted 18 February 2005
Available online 19 March 2005

Abstract

The structure of barium–titanium–metaborate $xBaO–xB_2O_3–yTiO_2$ ($y = 0\%$, 4%, 8%, 16% and $x = 50–y/2$) amorphous and crystallized powders, obtained using a polymeric precursor method, was investigated by Ti and B *K*-edge X-ray absorption spectroscopy (XAS) and ^{11}B-NMR high-resolution techniques. XANES study of amorphous samples shows that Ti^{4+} ions exist as $^{[4]}Ti$ species associated to $^{[6]}Ti$ and $^{[5]}Ti$ species in a practically equivalent amount. After crystallization, titanium environment is predominately composed by $^{[6]}Ti$ species. According to XANES results obtained at the B *K*-edge, the fraction of boron in tetrahedral sites ($^{[4]}B$) reduces as the amount of TiO_2 is increased from $x = 0\%$ to 4%, with a consequent increase of boron in trigonal sites ($^{[3]}B$). By a combination of ^{11}B-NMR spin-echo and triple quantum magic angle spinning (3Q-MAS) techniques, the detailed borate speciation was determined as consisting in $^{[4]}B$ and two kind of trigonal sites, $^{[3]}B_A$ and $^{[3]}B_B$, corresponding, respectively, to borates sharing three and two O atoms with other boron units. NMR results reveal not only the reduction in boron coordination also seen by XANES but also the simultaneous reduction in the condensation degree of trigonal units, when the Ti content is increased in the glass. In crystallized samples, β-BaB_2O_4 and $BaTi(BO_3)_2$ phases were identified and quantified by ^{11}B-NMR.

Keywords: Polymeric precursor method; $BaO–B_2O_3–TiO_2$; Powder; XANES; ^{11}B-NMR

1. Introduction

Barium metaborate crystal (β-BaB_2O_4 or β-BBO) is an important material for nonlinear optical applications in the visible and ultraviolet regions [1–3]. Its physical properties, such as a large effective second harmonic generation coefficient, wide range transparency, broad phase matched region and high damage threshold are suitable for many optical applications [4].

In the last decade, glass-ceramic materials, containing β-BBO phase were obtained from the crystallization of the $BaO–B_2O_3–TiO_2$ vitreous system [5,6]. According to these works, the difficulties in obtaining β-BBO phase from stoichiometric $50BaO–50B_2O_3$ compositions were overcome by adding TiO_2 compound to the $BaO–B_2O_3$ system. Although the vitreous phase contains a large quantity of TiO_2 (up to 16% in mole), the β-BBO phase was found to be the major phase when the glassy sample was subjected to the isothermal crystallization process [5,6].

The system $BaO–B_2O_3–TiO_2$ seems interesting for the manufacture of ferroelectric barium titanate glass-ceramic materials [7,8]. Moreover, a new approach for the chemical synthesis of powders to be used as target and thin films, based on a method developed by Pechini [9], has been extensively used to produce a large variety of materials [10–12]. This method is based on chelation

*Corresponding author. Fax: +55 16 3373 9824.
E-mail address: valmor@if.sc.usp.br (V.R. Mastelaro).

0022-4596/$ - see front matter © 2005 Elsevier Inc. All rights reserved.
doi:10.1016/j.jssc.2005.02.014

or complexion of cations by a hydrocarboxylic acid such as citric acid [9]. Compared to other chemical methods, the polymeric precursor method, or Pechini's method, offers the advantage of using common reagents and does not require a special atmosphere. Moreover, the nanometric powders obtained from such method can then be used as a source in different physical methods of thin film deposition. In a previous work [13], we used the polymeric precursor method to synthesize the β-BBO nanometric powder phase from the ternary xBaO–x-B_2O_3–yTiO$_2$ system (BBT), where $y = 4\%$, 8%, 16% and $x = 50—y/2$ (mol%) [13]. The β-BBO phase was found to be the main phase in samples containing $y = 4\%$ of titanium oxide. Recently, we used the nanopowder produced by this method to prepare thin films from the β-BaB_2O_4 composition using a electron beam evaporation method [14].

Although the synthesis and the properties of the BaO–B_2O_3–TiO$_2$ system have been widely exploited, little information is found in the literature concerning the structural role of TiO$_2$ on the BaO–B_2O_3 system, especially in samples prepared by a chemical solution method [13].

The aim of this work was to characterize the local order of Ti and B atoms in BBT amorphous powders, obtained from a polymeric precursor method [9], and also in recrystallized samples. To obtain a detailed description of the local structural parameters and the borate speciation, two experimental techniques were applied: the X-ray absorption spectroscopy (XAS) of Ti *K*-edge and B *K*-edge and solid-state ^{11}B nuclear magnetic resonance (NMR).

2. Experimental procedures

2.1. Materials

The powder samples in the xBaO–xB$_2$O$_3$–yTiO$_2$ system were prepared using the polymeric precursor method (Pechini Method) [9], with compositions $y = 0\%$, 4%, 8%, 16% and $x = 50-y/2$) (mol%). Barium citrates were formed by the dissolution of barium carbonate in an aqueous solution of citric acid. After the Ba-citrate solution was homogenized, a stoichiometric amount of titanium isopropoxide (in accordance with the three aforementioned compositions) was added to the Ba-citrate solution. The solution was kept under slow stirring for approximately 3 h and its pH was adjusted to a 2–3 interval. After homogenizing the solution containing the Ba and Ti cations, sorbitol and boric acid (99.8%) were dissolved in water and added to the solution citrates. The heat treatments to produce powder samples were carried out in two stages: initial heating to 330 °C/5 h in an oxygen atmosphere at a heating rate of 10 °C/min to pyrolize the organic materials, followed soon thereafter by heating to 450 °C for 20 h and 750 °C for 2 h. According to TGA analysis carried out in a previous study [13], there is no mass loss at the highest temperature in these samples, which means that the compositions are close to the batched compositions.

Polycrystalline and amorphous BaTi(BO$_3$)$_2$ powdered samples were used as structural references. These samples were prepared by mixing appropriate amounts of commercial powders of reagents grade BaCO$_3$, TiO$_2$ and B_2O_3, and then melted in a platinum crucible in an electrically heated furnace for 3 h at 1100 °C. The melt was quenched on a steel plate and annealed in a furnace at 450 °C for 1 h. To obtain a crystalline sample, the glass sample was heat-treated in air at 620 °C during 120 h.

From previous X-ray diffraction analysis of the samples crystallized at 750 °C for 2 h [13], the β-BaB_2O_4 (β-BBO) phase was found to be the main phase in all samples. Two other crystalline phases, BaTiO$_3$ and BaTi(BO$_3$)$_2$, were observed as secondary phases. The amount of BaTiO$_3$ decreases and that of BaTi(BO$_3$)$_2$ increases as the amount of TiO$_2$ increases. According to the solid equilibrium phase diagram given by Zhang et al. [15], the BaTiO$_3$ should not be observed for the range of our compositions. The formation of BaTiO$_3$ can be related to the deficiency of B_2O_3 compound. However, we can exclude the possibility of B_2O_3 loss in this range of temperatures according to TGA analysis [13]. Therefore, we attribute the formation of BaTiO$_3$ mainly to local non-homogeneities related to the presence of remnant organic moieties resulting of partial hydrolysis of Ti-isopropoxide in the early stages of the reaction. In any case, the small amount of BaTiO$_3$ inferred by DRX (less than 4%) indicates the small effect of these inhomogeneities.

2.2. XAS data collection and analysis

Ti *K*-edge absorption spectra were collected at the LNLS (Laboratório Nacional de Luz Sincrotron, Campinas, Brazil) facility using the XAS beam line [16]. The LNLS storage ring was operated at 1.37 GeV with a nominal ring current of 130 mA. Data were collected at the Ti *K*-edge (4966 eV) and Ba L_{III}-edge (5247 eV) in transmission mode using a Si (1 1 1) "channel-cut" monochromator. Ionization chambers were used to detect the incident and transmitted flux. An energy step equal to 0.4 and 1.0 eV was used to collect data at the near region of the absorption edge. Due to the low critical energy of the machine, harmonic contamination from the monochromator is negligible at the energy of measurements [16]. To monitor the energy calibration, the X-ray absorption near-edge structure (XANES) spectra of a metallic foil was recorded at the same time as XANES spectra of the samples, using a

third ionization chamber. The vertical slits were adjusted in order to obtain the best resolution. To compare the intensity and the position of the pre-edge features, all the XANES spectra were background corrected and normalized on the first X-ray absorption fine structure (EXAFS) oscillation.

X-ray absorption spectroscopy (XAS) measurements at the B *K*-edge were performed at LURE on the SuperACO storage ring (Orsay), which operated at 800 MeV energy with currents ranging from 215 to 400 mA. The XANES spectra have been measured on the SA22 beam line equipped with a high-energy plane grating spherical mirror monochromator, with a resolution of ~100 MeV at the B *K*-edge (188 eV). The energy of the monochromator was calibrated at the boron *K*-edge using the BN compound. The spectra were collected at room temperature using the fluorescence yield (FY) mode.

2.3. NMR data collection and analysis

High-resolution ^{11}B-NMR measurements were carried out at 9.4 T with a Varian Unity INOVA spectrometer, with magic-angle sample spinning (MAS) of up to 9 kHz in silicon nitride rotors. The NMR spectra were obtained with two pulse sequences in order to compare the reliability of the results. FID signals were obtained from applying the single pulse (SP) technique with $\pi/18$ pulses. Also, spin-echo (SE) experiments were carried out under MAS using the sequence proposed by Dumazy et al. [17] for spin $I = \frac{3}{2}$, which minimizes spectral distortions arising from ill-refocused signals (transients and anti-echoes). Echoes were generated from two low power pulses ($\gamma B_1 = 2$ kHz) of 9 and 18 μs separated by 15 μs delay and phase-cycled according to Ref. [18]. The spectra were obtained from the Fourier transform of the decaying part of the echoes. Up to 20,000 echo signals were collected. Numerical exponential filters of 30 Hz broadening were applied. Triple quantum-MAS NMR experiments (3Q-MAS) were carried out using two pulses for generation-reconversion of 3-quantum coherences into observable ones [18], with durations of 10 and 2.2 μs, respectively and intensity of 80 kHz. An additional Z-filter selective pulse of 11 μs length and 5 kHz strength was also applied [19]. Spectral widths of 30 and 64 kHz were used, respectively, for the direct and indirect dimensions. A number of 256 hypercomplex FID signals were collected, with 2048 points and 48 transients each. Recycle delays of 2 s were used in experiments on glassy samples, while 400 s were used in recrystallized samples. An aqueous solution of H_3BO_3 (0.1 M) was used as a reference for ^{11}B chemical shifts and radio frequency pulse power calibrations. The ^{11}B-NMR powder lineshapes associated to the central transition were simulated considering the inhomogeneous broadening caused by the second-order quadrupolar interaction under MAS [20]. For these simulations, a FORTRAN90 code was written for calculation of the spectral density of a powder sample and their convolution with a Gaussian/Lorentzian line, accounting for the distribution of coupling parameters in the disordered solid, the residual spin interactions and the homogeneous broadening.

3. Results

3.1. XANES results: Ti K-edge

The pre-edge region of the *K*-edge XANES spectra of some transition metal oxides are characterized by a pronounced feature several volts before the main rising edge. In transition metal oxides which crystallize in centrosymmetric structures, this pre-edge feature is very small or absent; in non-centrosymmetric structures it can be quite large. This pre-edge feature before the main edge is commonly attributed to transitions from 1*s* energy levels of Ti to the Ti3*d*/O2*p* molecular orbital [21–24]. A $1s \rightarrow 3d$ transition is Laporte forbidden by dipole selection rules but becomes allowed when *p–d* orbital mixing occurs such in a TiO_4 tetrahedron or a ($^{[5]}$TiO)O_4 site (i.e., without a center of symmetry) [21]. The height and position of this pre-edge feature are direct functions of the degree of *p–d* mixing, site distortion, oxidation state and experimental resolution [21–24].

Recently, Farges et al. [23,24] showed empirically that the average coordination number of Ti in a range of titanium oxide reference materials and titanium silicate glasses can be extracted reasonably well from plots of pre-edge intensity versus peak positions. Indeed, 4-, 5- and 6-fold coordinated Ti atoms appear to give pre-edge peaks at 4969.5, 4970.5 and 4971.5 ± 0.2 eV, respectively.

Fig. 1a shows the Ti *K*-edge XANES spectra of BBT amorphous samples heat treated at 450 °C during 20 h, whose amorphous state was checked previously by X-ray diffraction measurements [13]. The characteristic of the pre-edge structure for these amorphous samples is given in Table 1. The pre-edge structure in all the amorphous samples presents a unique and prominent peak around 4970.0 ± 0.2 eV, with intensity varying from 0.28 to 0.30. Based on the work of Farges [23,24], we can say that the pre-edge feature of this series of samples is characteristic of a mixture of $^{[4]}$Ti, $^{[5]}$Ti and $^{[6]}$Ti species. We did not observe a significant increase of the TiO_4 groups as the amount of titanium increases, as was observed by De Pablos et al. [25] in the B_2O_3–TiO_2–M_nO_m (M = Li, Ba, Pb) glassy systems.

Fig. 1b shows the Ti *K*-edge XANES spectra of BBT powders samples heat treated at 750 °C during 2 h. For comparison, we included in the figure the XANES spectrum of $BaTi(BO_3)_2$ and $BaTiO_3$ crystalline phases

because these two phases have been detected by previous XRD experiments [13]. As can be seen, as the amount of TiO_2 increases the XANES spectrum of crystallized samples becomes similar to that of $BaTi(BO_3)_2$ crystalline phase, in good agreement with the XRD results.

The characteristic of the pre-edge structures for these crystallized samples and for the $BaTi(BO_3)_2$ crystalline phase are also given in Table 1. As observed in the amorphous samples, the main structure at the pre-edge region is located at around 4970.3 ± 0.2 eV in all heat-treated samples. However, we observed a smaller decrease in its intensity for the $x = 16\%$ sample. As can be seen in Fig. 1, the XANES spectra of $x = 16\%$ sample and that of $BaTi(BO_3)_2$ sample are identical, which means that the environment of Ti atoms is similar on both samples. On the other hand, the same is not true for the $x = 4\%$ and 8% samples, where the amount of $BaTiO_3$ phase is more significant and should be taken into account. We know that Ti atoms in $BaTi(BO_3)_2$ are located in regular octahedra [15] whereas in the $BaTiO_3$ phase they are in distorted tetragonal environments, with one Ti–O bond located at 1.83 Å, four Ti–O bonds at 2.0 Å and one Ti–O bond at 2.21 Å [21]. As the intensity of the pre-edge peak at the Ti *K*-edge that we analyzed in our work can be directly related to the distortion of Ti site, we can infer that the smaller decrease observed on the pre peak intensity of the 16% TiO_2 sample is due to a decrease on the distortion of the Ti site. The analysis of the pre-edge feature position and intensity using the Farges' model indicates that we have

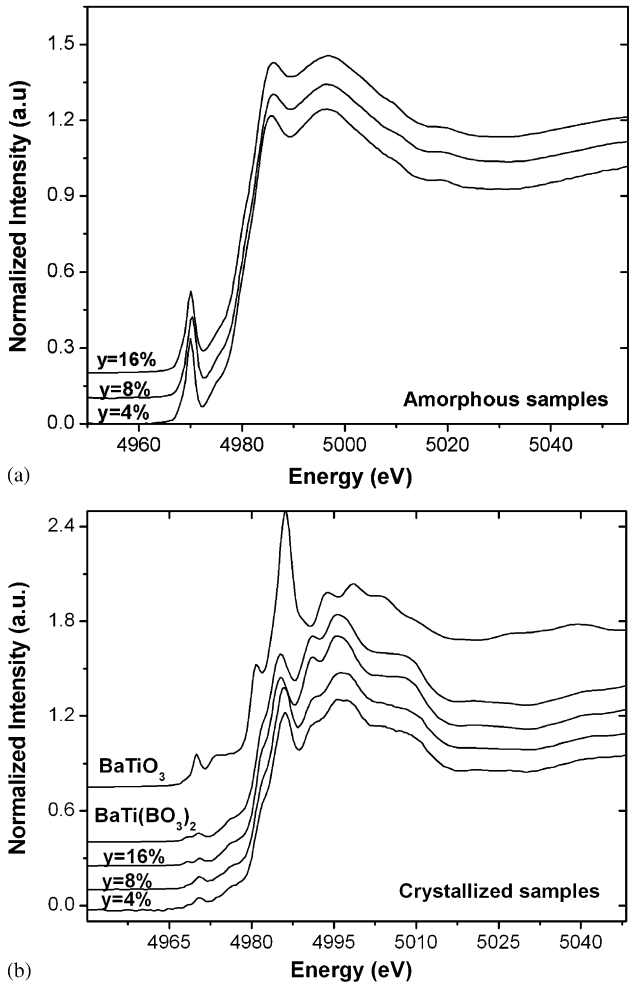

Fig. 1. Normalized Ti *K*-edge XANES spectra of (a) amorphous and (b) crystallized samples at 750 °C/2 h.

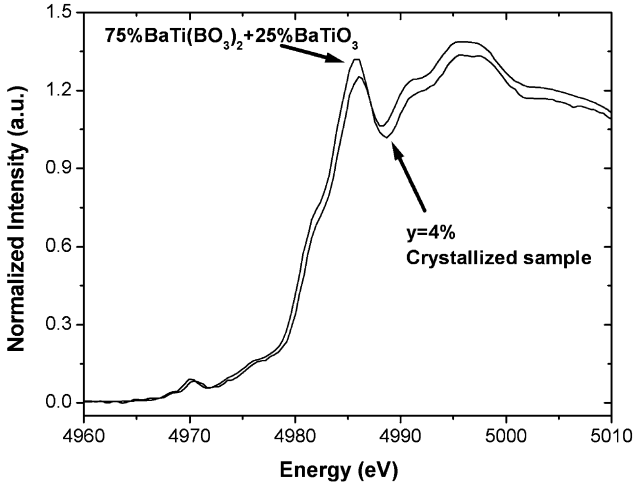

Fig. 2. Comparison between the Ti *K*-edge XANES spectrum of $y = 4\%$ amorphous sample with a XANES spectrum composed of a linear combination of 75% of the XANES spectrum of $BaTi(BO_3)_2$ and 25% of the XANES spectrum of $BaTiO_3$ crystalline phases.

Table 1
Position and intensity of structures at Ti pre-edge region and comparison with amorphous and crystalline phases and Ti species

Crystalline phases [8]	Sample	Position (eV) ±0.2 eV	Normalized height (a.u.)	Ti species
Amorphous	$y = 4\%$ TiO_2 450 °C/20 h	4970.0	0.30	$^{[4]}$Ti, $^{[6]}$Ti, $^{[5]}$Ti
Amorphous	$y = 8\%$ TiO_2 450 °C/20 h	4970.2	0.28	$^{[4]}$Ti, $^{[6]}$Ti, $^{[5]}$Ti
Amorphous	$y = 16\%$ TiO_2 450 °C/20 h	4970.0	0.28	$^{[4]}$Ti, $^{[6]}$Ti, $^{[5]}$Ti
β-BBO + $BaTiO_3$	$y = 4\%$ TiO_2 750 °C/2 h	4970.4	0.05	$^{[6]}$Ti, $^{[4]}$Ti, $^{[5]}$Ti
β-BBO + $BaTiO_3$ + $BaTi(BO_3)_2$	$y = 8\%$ TiO_2 750 °C/2 h	4970.4	0.05	$^{[6]}$Ti, $^{[4]}$Ti, $^{[5]}$Ti
β-BBO + $BaTiO_3$ + $BaTi(BO_3)_2$	$y = 16\%$ TiO_2 750 °C/2 h	4970.2	0.03	$^{[6]}$Ti, $^{[4]}$Ti, $^{[5]}$Ti
$BaTi(BO_3)_2$	$BaTi(BO_3)_2$	4970.3	0.04	$^{[6]}$Ti,

for the crystallized samples a mixture of $^{[6]}$Ti, $^{[5]}$Ti, $^{[4]}$Ti species, being the $^{[6]}$Ti species the predominant one.

Regarding the sample containing only 4% of TiO_2, according to previous XRD experiments, this sample only contains the $BaTiO_3$ and β-BBO phases [13]. However, if we compare the XANES spectra of $y = 4\%$ sample with that of $BaTiO_3$ (Fig. 1b), we can see a large difference between both XANES spectra, indicating that there are other crystalline phases containing titanium atoms contributing to the XANES spectra. The most evident possibility is the presence of $BaTi(BO_3)_2$. To verify this hypothesis, we compare the XANES spectra of $y = 4\%$ sample after crystallization with a linear combination of experimental XANES spectra of $BaTiO_3$ and $BaTi(BO_3)_2$ crystalline samples. As can be seen in Fig. 2, an excellent agreement was achieved with a simulated XANES spectra composed of 75% from $BaTi(BO_3)_2$ phase and 25% from $BaTiO_3$ phase. Thus, despite XRD results for the 4% TiO_2 sample only show the presence of β-BBO and $BaTiO_3$ crystalline phases, the XANES results also showed the presence of $BaTi(BO_3)_2$ phase, which is expected from the phase diagram of this system [15]. The non-observation of this phase through XRD could be attributed to the very small size of the crystallites, below the detection threshold of this technique.

3.2. XANES results: B K-edge

B *K*-edge XANES spectra of BBT powder samples heat-treated at 450 °C during 20 h are shown in Fig. 3. These spectra were normalized by I_0, corrected for a linear pre-edge background and then normalized again to the height of peak *A* in the spectrum of the sample with 0% of TiO_2, which corresponds to β-BBO. In agreement with other works [26–28], the B *K*-edge XANES spectra of BBT samples are dominated by three features, that are presently labeled *A*, *B* and *C* in Fig. 3. The sharp peak *A* is attributed to trigonal B and assigned to transition of B 1*s* electrons to unoccupied B $2p_z$ (Π^*) states of BO_3 groups [26–28]. Similarly, the peak B is attributed largely to tetrahedral $^{[4]}$B and assigned to transition of B 1*s* electrons to the unoccupied B σ^* states of BO_4 groups. The broad feature *C* reflects contributions from both trigonal BO_3 and tetrahedral BO_4 groups; it is assigned to transition of B 1*s* electrons to unoccupied B σ^* states of BO_3 groups and multiple scattering resonance.

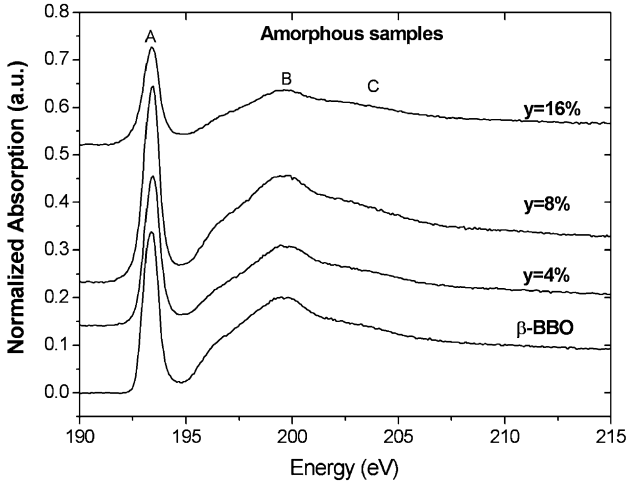

Fig. 3. Normalized B *K*-edge XANES spectra of amorphous samples obtained 450 °C/20 h.

Sauer et al. [29] and Garvie et al. [30] determined the proportion of tetrahedral $^{[4]}$B from the ratio of the area of peak *A* to the total area over an energy window from peak *A* to 14.6 eV above it, normalized by same ratio for a standard with 100% $^{[3]}$B. This total area method yielded consistent results for samples containing a moderate and/or low concentration of boron, but failed at high concentrations. To resolve this problem of background variation, Fleet and Muthupari [26] proposed a further procedure: a linear background extending from the base of peak *A* to the envelope at 20 eV above *A* was subtracted and the remaining spectrum was fitted to 5 Gaussian components, one for *A*, two for *B* (B_1, B_2), and two for *C* and the region beyond it. The fraction of tetrahedral boron was then given from the fitted peak area ratio $(B_1 + B_2)/(A + B_1 + B_2)$. Fig. 4 shows, as an example, the fitting procedure applied to the XANES spectra of β-BBO sample. The proportions of tetrahedral boron thus obtained from XANES spectra are given in Table 2. These values indicate that,

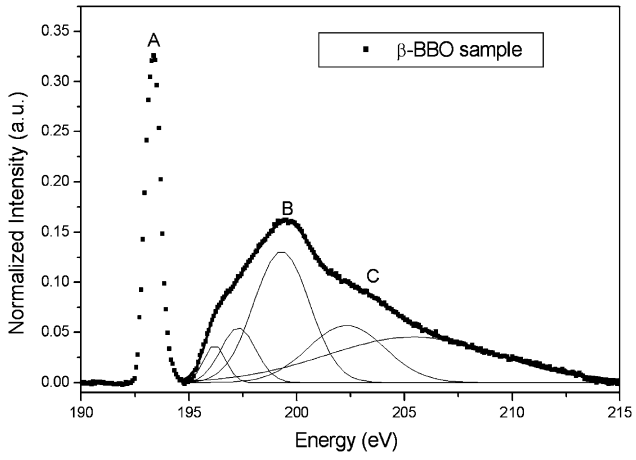

Fig. 4. Experimental and deconvoluted B *K*-edge XANES spectra for the β-BBO sample.

Table 2
Fractions of $^{[4]}$B as a function of the TiO_2 content *y*

y (%)	0 (β-BBO)	4	8	16
$^{[4]}$B fraction	0.69	0.61	0.62	0.60

between 0% (β-BBO) and 4% TiO_2 the fraction of tetrahedral sites changes from 0.69 to 0.61 with a consequent increase on the fraction of trigonal sites. However, we did not observe a significant change when the amount of TiO_2 increases to 8% or 16% (0.61 and 0.60 respectively). Similar results were obtained by Pernice et al. [5] when they studied the addition of TiO_2 in the $BaO–B_2O_3$ glassy system by Fourier transform infrared spectroscopy.

3.3. ^{11}B MAS NMR results

As boron has an important role on the physical properties of this glass system, we also characterize the local order around B atoms in glass and crystallized samples by means of high-resolution ^{11}B-NMR. The technique was applied to determine the fraction of boron species (tetrahedral and trigonal) and to get information about the atomic environments around these sites. Both aims depend on the careful determination of three NMR coupling parameters of ^{11}B nuclei on each site: (i) the quadrupolar coupling parameter χ between the electric field gradient (efg) on the site and the electric quadrupole moment of the ^{11}B nucleus, (ii) the asymmetry parameter η of the efg tensor and (iii) the isotropic chemical shift δ_{iso} [31]. In this work, a strategy combining triple quantum-MAS-NMR and properly phase-cycled spin-echo techniques was adopted to determine the interaction parameters and the site populations, followed by numeric simulations of the central transition NMR line shape.

Firstly, we compared the ^{11}B spectra obtained using SP and SE NMR techniques. Fig. 5a shows high-resolution NMR spectra of the Ti-free amorphous sample, obtained from both methods. It is possible to note some differences between these spectra. The decaying edges of the SP spectra are broader that those of the SE spectra. This kind of distortion arises mainly from dead-time problems at the beginning of the FID. On the other hand, SP spectra show lower intensities than SE spectra at central frequencies. This fact may result as a consequence of the line broadening mentioned above, and from the partially selective excitation of the quadrupolar powder pattern. In contrast, the spectrum obtained from SE is not affected by dead-time and the pulse sequence used in these experiments warrants a uniform excitation of the quadrupolar pattern [17]. Though small, the differences observed in Fig. 4a are non-negligible, and may affect seriously the values of intensities and interaction parameters obtained from spectral simulations. These distortions were systematically observed in the SP-spectra of all samples. Therefore, only spectra obtained from SE signals were considered in this study. Figs. 6a and 7a show the spectra corresponding to the set of amorphous and crystallized powders. We will discuss first the results obtained in amorphous samples.

The presence of $^{[3]}$B and $^{[4]}$B can be readily observed in the amorphous samples, the latter specie being the main responsible from the intense signal around –18 ppm. An unambiguous resolution of these sites can be obtained by means of the two-dimensional ^{11}B-3Q-MAS experiment. This experiment allows the separation of the NMR lines from both boron units along the indirect isotropic dimension, due to the lower quadrupolar coupling constant and more shielded chemical shift of $^{[4]}$B compared with $^{[3]}$B species. Fig. 8 shows a typical 3Q-MAS spectra for the amorphous powders,

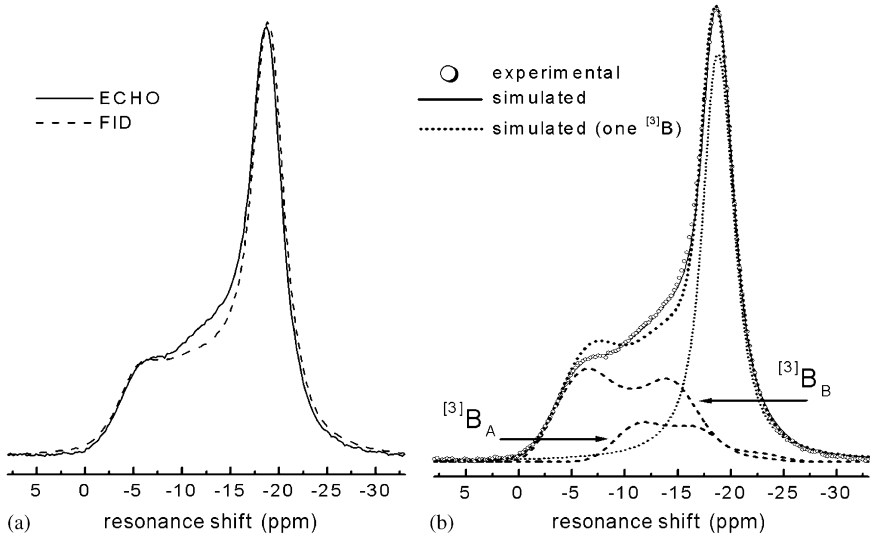

Fig. 5. ^{11}B-MAS NMR spectrum of the amorphous sample with 0% TiO_2. (a) Spectra obtained from spin-echo (solid line) and FID (dashed line). (b) Simulations of the spin-echo spectrum. Solid line: simulation with two trigonal species (dashed lines) and one tetrahedral (dotted line). Short dashed line: simulation with one trigonal and one tetrahedral.

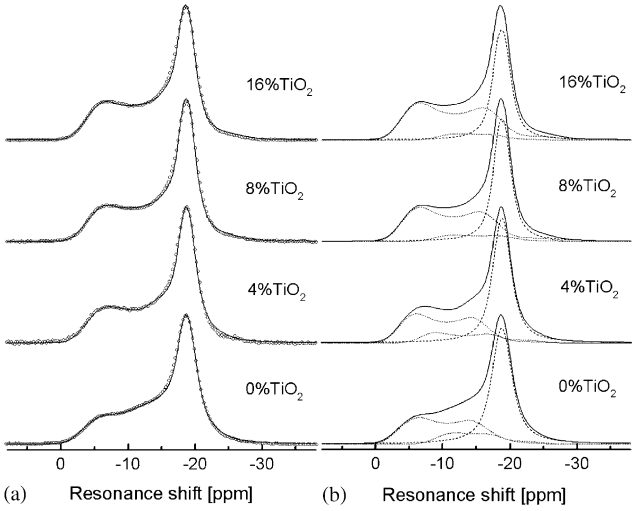

Fig. 6. ^{11}B-MAS spin-echo spectra of the amorphous samples. (a) Circles: experimental data. Solid line: simulation with two trigonal species and one tetrahedral. (b) Detail of the simulation components. Dotted lines: trigonal boron species. Dashed line: tetrahedral boron.

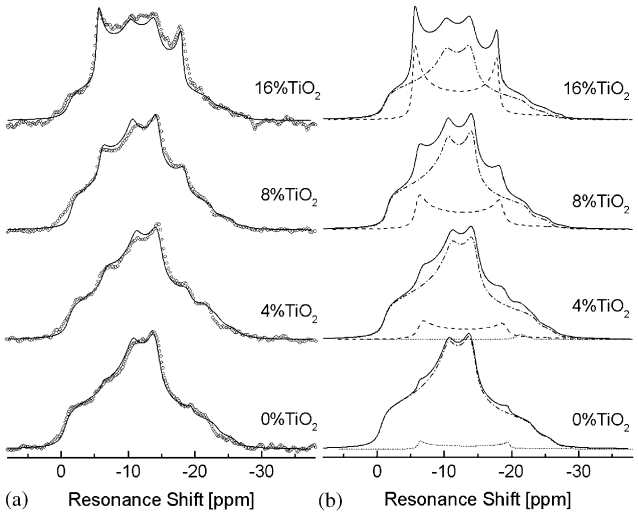

Fig. 7. ^{11}B-MAS spin-echo spectra of heat-treated samples. (a) Circles: experimental data. Solid line: simulations with trigonal sites from β-BBO and $BaTi(BO_3)_2$ crystal phases. (b) Detail of the simulation components. Dash-dot line: β-BBO. Dashed line: $BaTi(BO_3)_2$. Dotted line: glass.

corresponding to 16% of TiO_2, with projections along the isotropic and anisotropic axes. The 3Q-MAS spectra from amorphous samples show two intense and well-resolved peaks corresponding to $^{[3]}$B and $^{[4]}$B, respectively at high and low frequency along the isotropic dimension. The signal from $^{[3]}$B sites is broader than from $^{[4]}$B sites along the anisotropic axis, due to the stronger quadrupolar coupling. The isotropic chemical shift δ_{ISO} and the quadrupolar coupling

$$Pq = \chi\sqrt{1+\frac{\eta^2}{3}}$$

can be calculated for both sites, using the measured values for peaks frequencies [18]. The resulting parameters for amorphous samples are shown in Table 3. Only a small increase in shielding for $^{[3]}$B in Ti-containing glasses with respect to the Ti-free sample can be noted, while no variation in δ_{iso} for $^{[4]}$B sites can be observed. The mean quadrupolar coupling is essentially independent of composition for both species in these amorphous samples.

As 3Q-MAS experiments are not quantitative, the simulation of 1-D spectra is mandatory to get the boron speciation in these samples and to determine the values of the efg parameters χ and η separately. The parameters determined from the 3Q-MAS experiments were used as initial guess values for $^{[3]}$B and $^{[4]}$B sites. The values for δ_{iso}, χ, η and line intensities were systematically varied in order to reproduce the experimental spectrum. Gaussian and Lorentzian convolution functions were considered for boron sites. The best agreement with the experimental spectra was obtained considering a Lorentzian function for $^{[4]}$B sites and a Gaussian for $^{[3]}$B sites. This particular choice of functions was determined from the line shape on the opposite edges of the spectra. From the magnitudes of the interaction parameters measured from 3Q-MAS it was concluded that the high-frequency edge of the spectra is determined only by the $^{[3]}$B line, i.e. there is negligible overlap on this side of the spectrum. There was no satisfactory agreement between the simulations and the spectral profile when a Lorentzian convolution function was used. Therefore, a Gaussian line was adopted for the convolution function of trigonal boron. Fig. 5b shows a typical result obtained from the simulations, for the 0% TiO_2 amorphous sample. Simulations with only one trigonal site were clearly not satisfactory, particularly in the middle region of the spectra. This fact was previously noted by Clayden et al. [32] in melt-quenched glasses with these compositions, but they were not able to find a satisfactory solution with two $^{[3]}$B sites. Simulations including another ^{3}B site were attempted with our data, starting with the same interaction parameters for both trigonal species. This condition was assumed because the difference between the set of parameters of both sites should be small, as the 3Q-MAS experiments could not resolve them. As can be seen in Fig. 5b, the agreement of these simulations with experimental spectra was notoriously better than in the case of a single trigonal site. The simulations with two $^{[3]}$B sites and one $^{[4]}$B for the other amorphous samples are plotted in Fig. 6b. The interaction parameters and intensities obtained from this procedure are shown in Tables 4 and 5 for $^{[3]}$B and $^{[4]}$B sites, respectively. The main difference between both $^{[3]}$B species is in the magnitude of δ_{iso}. The less abundant trigonal specie $^{[3]}B_A$ has a chemical shift of about -8 ppm, while the most abundant $^{[3]}B_A$ has a shift of about -1.5 ppm.

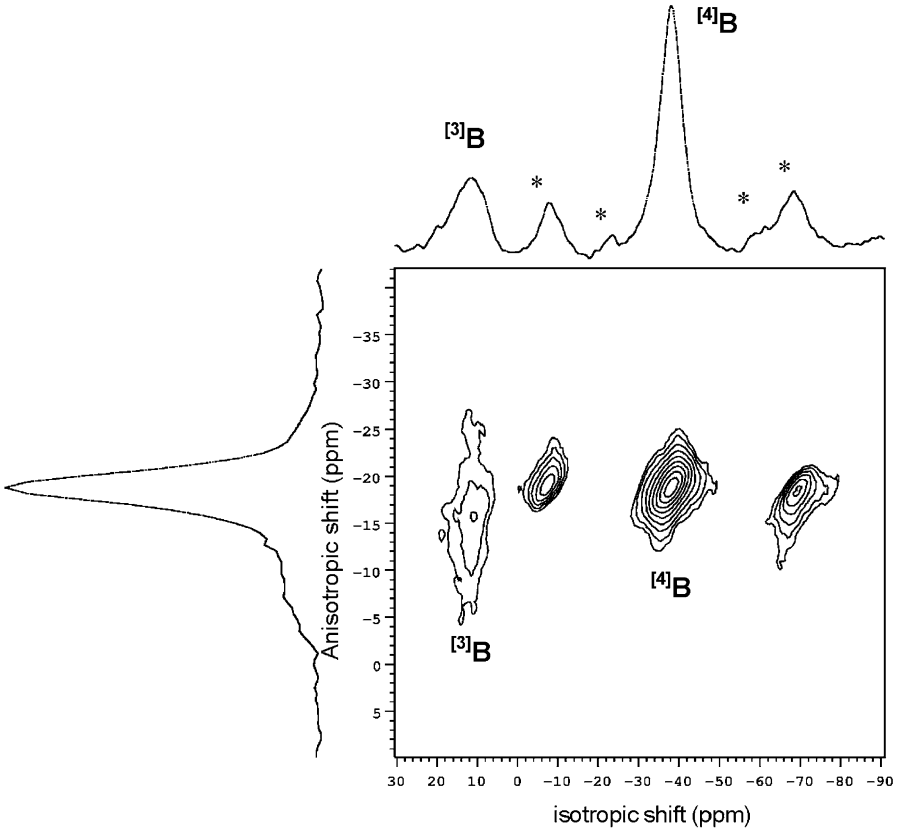

Fig. 8. ^{11}B-3Q-MAS spectrum of amorphous sample with 16% TiO_2.

Table 3
Interaction parameters of ^{11}B sites in amorphous powders obtained from 3Q-MAS-NMR experiments

Ti_2O (mol%)	δ_{iso} (ppm)		Pq (MHz)	
	$^{[3]}$B	$^{[4]}$B	$^{[3]}$B	$^{[4]}$B
0	−1.5±0.5	−17.9±0.4	2.8±0.1	0.90±0.05
4	−2.1±0.3	−18.0±0.3	3.0±0.1	0.90±0.05
8	−3.0±0.3	−18.3±0.2	3.1±0.1	0.90±0.05
16	−2.4±0.3	−18.2±0.2	3.1±0.1	0.90±0.05

Also, the quadrupolar coupling χ is slightly smaller for $^{[3]}B_A$ with respect to $^{[3]}B_B$. Comparing the interaction parameters measured from 3Q-MAS in Table 3 with the results of simulations, it can be seen a reasonable agreement for tetrahedral boron, considering the uncertainty of the methods. For the $^{[3]}B_A$ and $^{[3]}B_B$ sites, the difference in the populations observed in Table 4 can explain the fact that only one trigonal signal was observed in 3Q-MAS experiments. The $^{[3]}B_A$ fraction is three times smaller than $^{[3]}B_B$. Consequently, the measured values for δ_{iso} and P_q for the $^{[3]}$B site observed in 3Q-MAS are closer to those values of the most abundant $^{[3]}B_B$ specie. It can be noted that the value of η for these trigonal sites is between 0.2 and 0.3, clearly above zero, indicating distortions in both sites with respect to the C_3 symmetry.

According to Tables 3 to 4, there is no noticeable variation with the TiO_2 content of the coupling constant χ and chemical shift δ_{iso} for boron species. In contrast, the fraction of boron species shows systematic variations with composition. According to Tables 4 and 5, as the TiO_2 content increases there is a decrease in the $^{[4]}$B fractional population of 0.07, which represents a variation of 13% relative between the extreme compositions. Also, the fraction of $^{[3]}B_A$ species decreases in 0.07, which represents a decrease of about 50% relative to the 0% TiO_2 sample. Conversely, the fraction of $^{[3]}B_B$ increases by 0.14.

The nature of the two $^{[3]}$B species can be discussed in terms of δ_{iso}, the only interaction parameter that showed an appreciable difference between both trigonal sites. Kroeker and Stebbins showed that δ_{iso} in trigonal borates is sensitive to their condensation degree n, i.e. the number of B–O–B bridges per boron ($n = 0, 1, 2, 3$), though the increase in shielding per each bridge is only a few ppm [33]. Despite the overlap between chemical shift ranges for some values of n, the most connected trigonal unit ($n = 3$) is always the most shielded specie. In our measurements, $^{[3]}B_A$ sites have δ_{iso} values close to the higher limit of the most shielded values observed for

Table 4
Interaction parameters and populations of trigonal boron sites in amorphous powders obtained from the numerical simulation of spin-echo ^{11}B-MAS spectra

Ti_2O (mol%)	δ_{iso} (ppm)		χ (MHz)		η		Borate fraction	
	$^{[3]}B_A$	$^{[3]}B_B$	$^{[3]}B_A$	$^{[3]}B_B$	$^{[3]}B_A$	$^{[3]}B_B$	$^{[3]}B_A$	$^{[3]}B_B$
0	−7.2±0.4	−1.0±0.3	2.30±0.05	2.50±0.05	0.30±0.03	0.27±0.03	0.13±0.05	0.35±0.05
4	−7.0±0.4	−1.1±0.3	2.40±0.05	2.50±0.05	0.20±0.03	0.23±0.03	0.15±0.05	0.35±0.05
8	−7.5±0.5	−2.0±0.5	2.3±0.1	2.60±0.05	0.27±0.03	0.23±0.03	0.07±0.05	0.43±0.05
16	−8.5±0.5	−1.5±0.5	2.1±0.1	2.10±0.05	0.27±0.03	0.20±0.03	0.06±0.04	0.49±0.05

Table 5
Interaction parameters and populations of tetrahedral boron sites in amorphous powders obtained from the numerical simulation of spin-echo ^{11}B-MAS spectra

Ti_2O (mol%)	δ_{iso} (ppm)	χ (MHz)	η	Borate fraction
	$^{[4]}B$	$^{[4]}B$	$^{[4]}B$	$^{[4]}B$
0	−17.4±0.2	0.96±0.02	0.00±0.01	0.52±0.04
4	−17.5±0.2	0.95±0.02	0.00±0.01	0.50±0.04
8	−18.1±0.2	0.96±0.02	0.00±0.01	0.50±0.05
16	−18.0±0.2	0.97±0.02	0.00±0.01	0.45±0.05

trigonal boron in Ref. [33], from −2.5 to −6 ppm, indicating that $^{[3]}B_A$ species could be attributed to $n = 3$. The following least-shielded species are those with $n = 2$, ranging approximately from −1 to −2.5 ppm [33]. The measured shift for $^{[3]}B_B$ lies within this range, so we can attribute $n = 2$ for these boron sites. Kroeker and Stebbins pointed out that trigonal boron with $n = 2$ or $n = 3$ in rings are slightly less shielded than similar units in other arrangements. For this reason, and considering the extreme shielding observed of $^{[3]}B_A$ sites, we are led to conclude that most probably these units are not forming rings. With respect to $^{[3]}B_B$ units, the small difference in shielding within the $n = 2$ range precludes any conclusion whether rings are formed or not.

On the other hand, the ^{11}B spectra from heat-treated BBT powders presented features clearly distinctive of the quadrupolar interaction in polycrystalline samples (Fig. 7a). In a previous X-ray diffraction study on these samples, two crystalline phases containing boron were detected, β-BBO and $BaTi(BO_3)_2$, with concentrations depending on the sample composition [13]. For this reason, ^{11}B-NMR measurements were carried out in a bulk sample of $BaTi(BO_3)_2$, in order to determine with accuracy the interaction parameters, which were used in the simulations of the spectra from heat-treated samples. Fig. 9 shows the ^{11}B-NMR spectra of this reference sample and the numerical simulation, which gave the interaction parameters shown in Table 6 for the unique $^{[3]}$B site observed. For heat-treated powders, simulations of the ^{11}B-NMR spectra were done considering the

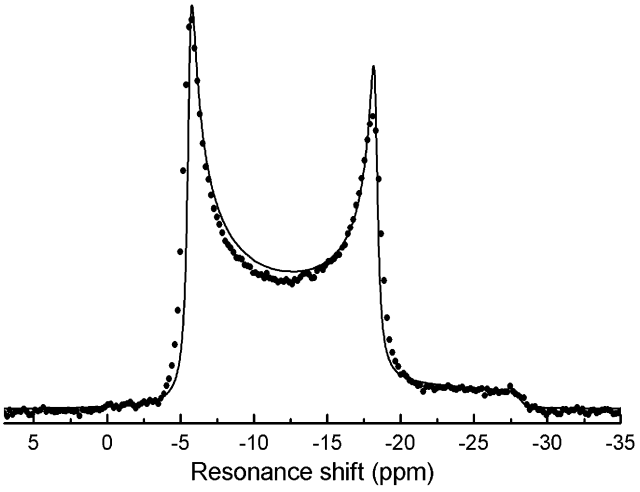

Fig. 9. ^{11}B-MAS spin-echo spectra of a polycrystalline sample of $BaTi(BO_3)_2$. Circles: experimental data. Solid line: simulation of the second-order quadrupole effects.

powder patterns of the crystal phases β-BBO and $BaTi(BO_3)_2$, allowing the variation of their relative intensity and interaction parameters. The resulting crystal fractions and site parameters are shown in Table 6, while the calculated spectra are shown in Fig. 7b. The resulting interaction parameters for $BaTi(BO_3)_2$ in crystallized powders are comparable with those measured in the bulk reference sample. The fraction obtained for β-BBO is in good agreement with previous X-ray diffraction results [13] considering the 5% uncertainty of that experimental determination. On the other hand, considering the equilibrium phase diagram, which predicts crystallization only of β-BBO and $BaTi(BO_3)_2$, the fractions of β-BBO phase can be calculated as 0.917, 0.826 and 0.619, for increasing TiO_2 concentrations. The NMR fractions are in reasonable agreement with these values. The largest fractional difference is observed for the 4% TiO_2 sample, where the NMR fraction is lower than the predicted one by 0.06. This difference could be the result of an overestimation of the $BaTi(BO_3)_2$ fraction due to some amount of remnant amorphous material, which has a broad resonance line of $^{[3]}$B species overlapping the

Table 6
Interaction parameters and crystal phase fractions in heat-treated powders obtained from the numerical simulation of spin-echo ^{11}B-MAS spectra

Ti_2O (mol%)	δ_{iso} (ppm)		χ (MHz)		η		Crystal phase fraction	
	β-BBO	$BaTi(BO_3)_2$	β-BBO	$BaTi(BO_3)_2$	β-BBO	$BaTi(BO_3)_2$	β-BBO	$BaTi(BO_3)_2$
0	−1.1±0.3	—	2.50±0.02	—	0.74±0.02	—	1	0
4	−1.7±0.3	−3.5±0.3	2.48±0.02	2.62±0.02	0.75±0.03	0.00±0.001	0.86±0.04	0.14±0.04[a]
8	−1.9±0.3	−3.0±0.3	2.45±0.02	2.62±0.02	0.70±0.03	0.00±0.001	0.78±0.04	0.22±0.04
16	−1.6±0.3	−2.5±0.3	2.46±0.02	2.62±0.02	0.70±0.03	0.00±0.01	0.63±0.04	0.37±0.04
$BaTi(BO_3)_2$		−2.5±0.2		2.635±0.003		0.00±0.01		

[a]Possibly overestimated due to overlap with NMR signal from the amorphous fraction.

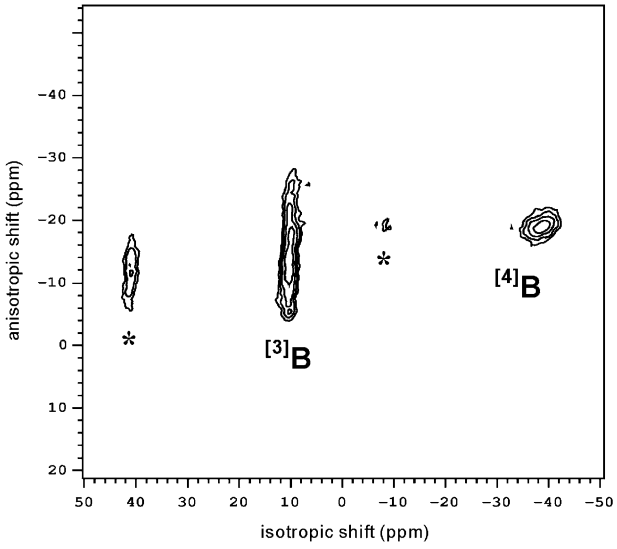

Fig. 10. ^{11}B-3Q-MAS spectrum of heat-treated powder sample with 8% TiO_2. The $^{[3]}$B trigonal site corresponds mainly to β-BBO crystal phase, while the $^{[4]}$B tetrahedral site corresponds to amorphous domains. Asterisks: spinning side-bands.

$BaTi(BO_3)_2$ resonance. Indeed, a total fraction of 0.04 of B in amorphous structure was detected in the simulation of the NMR spectrum of the 0% TiO_2 crystallized sample. In the 4% TiO_2 sample, a 0.008 fraction of $^{[4]}$B in amorphous structure was detected, demonstrating the existence of non-crystallized material in this sample too. As the associated $^{[3]}$B signal of the amorphous part is impossible to separate from the $BaTi(BO_3)_2$ line shape, then the calculated fraction of $BaTi(BO_3)_2$ for this sample could be overestimated by about 0.03, assuming a similar amorphous fraction as in the 0% Ti sample. For the crystallized samples with 8% and 16% TiO_2, no amorphous fractions could be detected, and crystal fractions calculated from NMR are closer to the expected values.

Fig. 10 shows a typical 3Q-MAS spectrum obtained in these heat-treated samples. In all samples, the most intense 3Q-MAS signal corresponds to $^{[3]}$B species in crystalline structure. These experiments show clearly that the fraction of tetrahedral boron is minimum, and can be attributed to remnant non-crystallized material. Table 7 shows the interaction parameters obtained from these experiments. The observed $^{[3]}$B site corresponds approximately to the β-BBO phase. The signal from $BaTi(BO_3)_2$ is not observed here because the ^{11}B spin–lattice relaxation time in this phase is several tens of seconds long, and the bi-dimensional spectrum was measured with a short recycle time (2 s) in order to give a reasonable experiment duration.

4. Discussion

According to the literature, the behavior of Ti cannot be described simply as a network former or modifier [34–36]. It was observed that Ti acts as a network former in systems with a significant amount of 4- and 5-fold coordinated species [34,35]. Thus, according to the coordination numbers extracted from the Ti *K*-edge XANES spectra of amorphous samples, we can state that Ti is partially acting as a network former in the BBT system.

On the other hand, XANES B *K*-edge results of the amorphous samples indicate a reduction of 0.09 in the fraction of $^{[4]}$B as the amount of TiO_2 is increased from 0% to 4%, representing a relative variation of 13%. This observation is in agreement with results obtained by Clayden et al. [32] in melt-quenched glasses using ^{11}B NMR. According to their work, the net effect of the addition of TiO_2 on the BO_4 fraction in the network will depend on the population balance between forming $TiO_{4/2}$ and modifier TiO_6^{2-} groups [32]. When titanium adopts 6-fold co-ordination as TiO_6^{2-}, requires a balancing charge from the Ba^{2+} cations. As a consequence, less charge is available to the borate network, which must polymerize further at the expenses of tetrahedral sites. For this reason, TiO_6^{2-} groups will favor the formation of trigonal boron units.

After crystallization, XANES results shows that $^{[6]}$Ti species become predominant and for the $y = 16\%$ sample, only the $BaTi(BO_3)_2$ phase is observed, in good agreement with previous XRD results [13]. In the case of sample containing 4% of TiO_2, from the XANES

Table 7
Interaction parameters of ^{11}B sites in thermally treated powders obtained from 3Q-MAS-NMR experiments

Ti_2O (mol%)	δ_{iso} (ppm)		Pq (MHz)	
	$^{[3]}B$ crystal β-BBO	$^{[4]}B$ amorphous	$^{[3]}B$ crystal β-BBO	$^{[4]}B$ amorphous
0	-1.2 ± 0.2	—	2.70 ± 0.05	—
4	-1.3 ± 0.2	-18.9 ± 0.3	2.75 ± 0.05	1.0 ± 0.2
8	-1.4 ± 0.2	-18.6 ± 0.2	2.70 ± 0.05	0.9 ± 0.2
16	-1.4 ± 0.3	-18.8 ± 0.2	2.70 ± 0.05	0.6 ± 0.2

results, it was possible to shown the presence of the $BaTi(BO_3)_2$ phase that had not been observed in XRD measurements [13].

The structural picture provided by ^{11}B-NMR is compatible with these observations. NMR results allow to determine the borate speciation in amorphous powders with greater detail, as consisting in $^{[4]}B$, $^{[3]}B_A$ and $^{[3]}B_B$ sites. A fraction of about 0.50 corresponds to $^{[4]}B$ species, which reduces by 0.07 in going from 0% TiO_2 to 16% TiO_2, equivalent to a relative variation of 13%. The more shielded $^{[3]}B_A$ sites correspond to highly connected borates, sharing their three O atoms with other boron units. The amount of these $^{[3]}B_A$ species reduces greatly with the increase of Ti content. At the same time, the fraction of less connected $^{[3]}B_B$ species, sharing two O with other boron atoms, increases at expenses of the more connected species. Therefore, NMR reveals not only the reduction in boron coordination detected by XANES, but also the simultaneous reduction in the condensation degree of trigonal units, when Ti content is increased. Both processes are compatible with the mechanism discussed above. The relative reduction in the fraction of $^{[4]}B$ units determined by NMR is compatible with the XANES results, although the absolute values are different, as can be seen comparing data in Tables 2 and 5. We believe that the fractions estimated from NMR data are less prone to systematic errors than XANES, provided that simulations are carried out on non-distorted spin-echo spectra. The separation from trigonal and tetrahedral signals is better in NMR spectra and the line shapes associated to the second-order quadrupole interaction are more constrained than XANES simulations.

On the other hand, these results are compatible with some conclusions obtained in a previous infra-red spectroscopy study on glasses of the same compositions prepared through melt-quenching process [5]. Increasing the Ti content from 0% to 4%, the decrease in the population of $^{[4]}B$ sites was also observed in that study, in addition to the increment in the population of a highly connected trigonal boron. However, from the qualitative analysis of the infra-red spectrum, these trigonal sites were attributed to species with $n = 3$ [5]. Our present NMR determination indicates that the majority of the trigonal sites corresponds to $n = 2$ species, according to the values of isotropic chemical shift. We believe that the NMR analysis has the advantage of a quantitative treatment of the spectra, which is not possible in the case of the broad infra-red spectra of these glasses.

The possible existence of differences between the short-range structure around B in amorphous powders and in melt-quenched glasses may be discussed. In a recent study, a determination of the borate speciation in BBT glasses was performed by NMR [32]. For the glasses with compositions containing the same amount of TiO_2 as our amorphous samples, the measured ^{11}B-NMR spectra show some differences with the present results. The intensity of $^{[4]}B$ signal for these glasses is greater than in spectra of amorphous powders. The total line-breath measured at the base of those spectra is 10ppm greater than in our amorphous powders, showing a Lorentzian-like profile at the edges and less resolution of details. Consequently, the borate speciation obtained from those spectra shows notorious differences with respect to our results, giving a population of about 25% of $^{[4]}B$. In order to check whether these observations are attributable to fundamental structural differences, we also prepared melt-quenched glasses for the three Ti-containing compositions [37]. These glass samples were prepared by using the conventional melt-quench technique. We performed ^{11}B spin-echo NMR experiments and the obtained spectra were almost identical to those observed in the amorphous samples [37]. Only a small broadening was observed, qualitatively similar to the spectra reported in Ref. [32] but still well below the line-breath values presented in that study. Also, it should be mentioned that the differences between spectra obtained from spin-echo or FID signals are quite small to take account of the difference with the spectra reported in Ref. [32]. Therefore, from our set of measurements we are led to conclude that there are no significant structural differences at molecular scale between the amorphous powders and bulk melt-quenched glasses with the same composition. The variance with respect to the results reported in Ref. [32] may be attributed to the preparation conditions of the melt-quenched glasses.

5. Conclusions

The combined application of XAS and NMR techniques provided a picture of the network organization and crystallization behavior in the $BaO–B_2O_3–TiO_2$ system for amorphous samples obtained using the Pechini method. Titanium ions enter as tetrahedral TiO_4 units, five and six-fold coordinated species. These highly coordinated species cause a depolimerization of the borate network, reducing the fraction of tetrahedral and trigonal ($n = 3$) species and increasing the fraction of less interconnected trigonal species ($n = 2$). No variations in the chemical shift or the electric field gradient around B atoms were observed with the addition of TiO_2, indicating that the geometry of the borate units is not appreciably distorted in this range of compositions. Also, no structural differences between these amorphous powders and bulk melt-quenched glasses of the same compositions were detected at the molecular scale around boron atoms.

Acknowledgments

Financial support from FAPESP through Grant 00/02805-6 is gratefully acknowledged. Research partially performed at LNLS—National Laboratory of Synchrotron Light, Brazil.

References

[1] C.T. Chen, B. Wu, A. Jiang, G. You, Sci. Sin. B28 (1985) 235.
[2] K. Kato, IEEE J. Quantum Electron. 22 (1986) 1103.
[3] K. Miyazaki, H. Sakie, T. Sato, Opt. Lett. 11 (1986) 797.
[4] S.Y. Stefanovich, V.N. Sigaev, Glass. Phys. Chem. 21 (1995) 253.
[5] P. Pernice, S. Esposito, A. Aronne, Phys. Chem. Glasses 39 (1998) 222.
[6] Y. Ding, A. Osaka, Y. Miura, J. Am. Ceram. Soc. 77 (1994) 749.
[7] A. Bhargava, J.E. Shelby, R.L. Snyder, J. Non-Cryst. Solids 102 (1–3) (1988) 136.
[8] K. Kusumoto, T. Sekiya, Y. Murase, Mater. Res. Bull. 28 (5) (1993) 461.
[9] M.P. Pechini, U.S. Patent No. 3.330.697, 1967.
[10] F.C.D. Lemos, E. Longo, E.R. Leite, D.M.A. Melo, A.O. Silva, J. Sol. State Chem. 177 (4–5) (2004) 1542.
[11] V. Bouquet, M.I.B. Bernardi, S.M. Zanetti, E.R. Leite, E. Longo, J.A. Varela, M.G. Viry, A. Perrin, J. Mater. Res. 15 (11) (2000) 2446.
[12] E.C. Paris, E.R. Leite, E. Longo, J.A. Varela, Mater. Lett. 37 (1–2) (1988) 1.
[13] L.J.Q. Maia, M.I.B. Bernardi, A.R. Zanatta, A.C. Hernandes, V.R. Mastelaro, Mater. Sci. Eng. B107 (2004) 33.
[14] L.J.Q. Maia, C.A.C. Feitosa, F.S. De Vicente, V.R. Mastelaro, M. Siu Li, A.C. Hernandes, J. Vac. Sci. Technol. A 22 (5) (2004) 2163.
[15] S.Y. Zhang, X. Wu, X.L. Chen, M. He, Y.G. Cao, Y.T. Song, D.Q. Ni, Mater. Res. Bull. 38 (2003) 783.
[16] H. Tolentino, J.C. Cesar, D.C. Cruz, V. Campagnon-Cailhol, E. Tamura, M.C.M. Alves, J. Synchrotron Rad. 5 (1998) 521.
[17] Y. Dumazy, J.-P. Amoreaux, C. Fernandez, Mol. Phys. 90 (1997) 959.
[18] D. Massiot, B. Touzo, D. Trumeau, J.P. Coutures, J. Virlet, P. Florian, P.J. Grandinetti, Sol. State. NMR 6 (1996) 73–83.
[19] J.-P. Amoreaux, C. Fernandez, S. Steuernagel, J. Magn. Reson. A 123 (1996) 116.
[20] F. Lefebvre, J.P. Amoreaux, C. Fernandez, E. Derouane, J. Chem. Phys. 86 (11) (1987) 670.
[21] B. Ravel, E.A. Stern, R.I. Vedrinskii, V. Kraizman, Ferroelectrics 206–207 (1998) 407.
[22] B. Ravel, E.A. Stern, Physica B 208–209 (1995) 316.
[23] F. Farges, J. Non-Cryst. Solids 204 (1996) 53.
[24] F. Farges, G.E. Brown Jr., J.J. Rehr, Geoch. Cosmoch. Acta 60 (16) (1996) 3023.
[25] De Pablos, A. Duran, Fundamentals of Glass Science and Technology. Proceedings of the Second Conference of the ESG 1993, Venice, Italy, p. 363.
[26] M.E. Fleet, S. Muthupari, J. Non-Cryst. Solids 255 (1999) 233.
[27] M.E. Fleet, S. Muthupari, Am. Miner. 85 (2000) 1009.
[28] M.E. Fleet, X. Liu, Phys. Chem. Miner. 28 (2001) 421.
[29] H. Sauer, R. Brydson, P.N. Rowley, W. Engel, J.M. Thomas, Ultramicroscopy 49 (1993) 198.
[30] L.A.J. Garvie, A.J. Craven, R. Brydson, Am. Miner. 80 (1995) 1132.
[31] M.E. Smith, E.R.H. Van Eck, Prog. Nucl. Mag. Res. 34 (1999) 159.
[32] N.J. Clayden, S. Esposito, A. Aronne, P. Pernice, J. Non-Cryst. Solids 249 (1999) 99.
[33] S. Kroeker, J. Stebbins, Inorg. Chem. 99 (2001) 6239.
[34] B.V.J. Rao, Phys. Chem. Glasses 4 (1963) 22.
[35] L. Cormier, P.H. Gaskell, G. Calas, A.K. Soper, Phys. Rev. B 58 (17) (1988) 11322.
[36] V.R. Mastelaro, R. Keding, J. Non-Cryst. Solids 282 (2001) 181.
[37] C.A. Feitosa, Ph. D. Thesis, University of São Paulo, 2004.